1 **Improving the accuracy in particle concentration measurements of a**
2 **balloon-borne optical particle counter UCASS**

3 Sina Jost[1], Ralf Weigel[1], Konrad Kandler[2], Luis Valero[2], Jessica Girdwood[3, 4], Chris Stopford[3],
4 Warren Stanley[3], Luca K. Eichhorn[1], Christian von Glahn[1], and Holger Tost[1]

5 [1]Institute for Physics of the Atmosphere, Johannes Gutenberg University, Mainz, Germany
6 [2]Institute for Applied Geosciences, Technical University Darmstadt, Germany
7 [3]Particle Instruments & Diagnostics Research Group, University of Hertfordshire, Hatfield,
8 Hertfordshire, AL10 9AB, United Kingdom
9 [4]National Centre for Atmospheric Science, School of Earth, Atmospheric and Environmental
10 Sciences, University of Manchester, Manchester, M13 9PL, United Kingdom
11
12 Corresponding authors: Sina Jost (sjost@students.uni-mainz.de) and Ralf Weigel, (weigelr@uni-
13 mainz.de)

1 Abstract

15 For balloon-borne detection of aerosols and cloud droplets (diameter $0.4 < D_\mathrm{p} < 40$ µm), a passive-
16 flow Universal Cloud and Aerosol Sounding System (UCASS) was used, whose sample flow rate is
17 conventionally derived from balloon ascent rates using GPS or pressure measurements.
18 Improvements are achieved by implementing thermal flow sensors (TFS) 94 mm downstream of
19 the UCASS detection region for continuously measuring true UCASS sample flow velocities.
20 UCASS-mounted TFS were calibrated during wind tunnel experiments at up to 10 m s^{-1} also under
21 various angles-of-attack (AOA), as these vary during actual balloon ascents. It was found that the
22 TFS-calibration is determined with sufficient precision using three calibration points at tunnel
23 flows of ~ 2, 5, and 8 m s^{-1}, simplifying efficient TFS-upgrades of numerous UCASS. In iso-axial
24 alignment, UCASS flows are accelerated (by ~ 11.3 %) compared to tunnel flows (at 2 – 8 m s^{-1}).
25 In-flight comparisons up to 7.5 km height revealed that UCASS sample flows rarely match the
26 balloon's ascent rate. Laboratory experiments show that equality ($v_\mathrm{GPS} = v_\mathrm{TFS}$) is achieved only at
27 AOA ≠ 0°, potentially affecting the UCASS-internal flow pattern and particle transmission efficiency
28 in flight. To minimise errors on calculated UCASS-based particle number concentrations, real-
29 time measurements of the true UCASS flow velocity are recommended.

2 Introduction

Weather balloon soundings are an established method to carry out in-situ measurements up to high altitudes in the atmosphere (e.g. Golden et al. (1986), Vömel and Fujiwara (2021), or Vömel and Ingleby (2023)). Balloons filled with helium or hydrogen can reach heights of up to 40 km. Due to a moderately variable ascent rate of ~ 5 - 6 m s^{-1} on average, the troposphere and stratosphere are probed with a higher vertical resolution compared to aircraft measurement due to the higher climb and descent rates of the latter (at least 6 m s^{-1} and usually more, cf. Eufar (2000)). In conventional operation, a radiosonde is used as payload deployed on a thin cord of about 50-60 m length below the ascending weather balloon. Radiosondes are used to directly measure atmospheric pressure, humidity, temperature, and wind parameters during the ascent, while the data are sent in real time via radio to the receiving station (see, e.g., Dirksen et al. (2020)).

Balloon-based vertical soundings with radiosondes allow for characterising the current state of the atmosphere, from which atmospheric properties such as stability or stratification can be derived. The payload of the weather balloon can be extended beyond the sole use of radiosondes, for example by including an ozone probe (cf. Smit et al. (2024) and references therein) and/or optical particle counters (Matsumura et al. (2001); Kasai et al. (2003); Smith et al. (2019); Kezoudi et al. (2021); Snels et al. (2021)). Both ozone, as an atmospheric trace gas, as well as aerosols and clouds have a major influence on the Earth system. Aerosols and clouds influence the Earth's energy balance (by absorbing and scattering short-wave radiation), the global water cycle (through the formation of precipitation) and the atmospheric dynamics (through the conversion of latent heat in the phase transitions of water). Considering, that aerosols and cloud droplets modify radiative fluxes (see, e.g., Stier et al. (2024) or IPCC (2023)), a better understanding of their size, number and vertical distribution is required and the vertical distribution of aerosols and cloud droplets need to be frequently investigated. The University of Hertfordshire (UK) has developed an optical particle spectrometer for balloon soundings: The "Universal Cloud and Aerosol Sounding System" (UCASS, see Smith et al. (2019); Kezoudi et al. (2021); Girdwood et al. (2022); Girdwood (2023), Schön et al. (2024)) is used to detect aerosol particles and cloud droplets with diameters of 0.4 to 40 μm. The probe's measuring principle is described in detail in Sect. 3.

In general, the thought model underlies the balloon sounding, that the horizontal wind that drifts the balloon or influences its geographical position has almost no or a negligible influence in the inertial system of the balloon itself, unless gusty winds or strong wind shear prevail. Hence, regarding the horizontal wind component, there is almost no relative horizontal wind aboard the balloon or its payload. The predominant flow relative to the balloon and its payload that mainly drives the air flow through a UCASS is the vertical wind component, which in our case is determined by the balloon's lift, i.e. its ascent rate.

To calculate a particle number concentration from the particle number detected (per unit time) by a balloon-borne UCASS, the sample volume flow rate through the UCASS detection region must be known. Conventionally, the sample volume flow was determined using balloon ascent rates (Kezoudi et al., 2021) derived from GPS or pressure measurements. This approach has two major disadvantages: a) a zero horizontal wind velocity is inherently assumed, and b) changes in airflow caused by the instrument housing, or small fluctuations remain unconsidered. One goal of this work therefore is to modify a UCASS such that a thermal flow sensor (TFS) is used to continuously determine the flow rates through a balloon-borne UCASS. This enables the accurate and precise

determination of particle concentrations (and inferred microphysical quantities) at a higher confidence level. Beyond that, this study is a prerequisite for investigations based on UCASS measurements during our balloon missions in Central Europe during summer of the years 2023 and 2024. Ultimately, the proposed improvements may provide support for UCASS applications by other users.

The present publication is structured as follows. First, the instrument is described. This is followed by reports on the testing and characterization of the method of mechanically coupling the TFS to the UCASS (Sect. 3.5.1). Subsequently, the experiments aiming at the optimum position of the TFS within the flow through a UCASS are described (Sect. 3.5.2). The TFS are then calibrated against a reference flow sensor (Prandtl pitot tube, PPt) within the flow through a UCASS (Sect. 3.5.3). Based on a numerical simulation, it has already been assumed that the flow velocity within the iso-axially aligned UCASS would increase by 12 % as compared to the ambient air flow speed of 5 m s^{-1} (Smith et al., 2019). Therefore, in this work the PPt-measured ambient flow velocities and TFS-detected flow velocity inside the UCASS are compared (Sect. 4.2). The impact of a non iso-axial alignment (i.e. when the angle of attack, AOA, towards the UCASS varies due to the balloon-payload's pendulum motion) on the flow velocities through the UCASS and on the TFS calibration curves are investigated (Sect. 4.3 and 4.4). Finally, balloon soundings with the UCASS - TFS combination are used to prove the TFS performance under atmospheric conditions (Sect. 5). The findings are summarised in the conclusion section.

3 Instruments and methods

3.1 Universal Cloud and Aerosol Sounding System (UCASS)

The UCASS is an optical particle spectrometer (nominal detection range $0.4 < D_\mathrm{p} < 40$ μm; Smith et al. (2019), Girdwood (2023)). Due to its small size, low weight and comparatively low cost (approx. 2700 € per unit), the UCASS is well suitable for balloon soundings. The UCASS is of tubular shape with 183 mm in length and with an outer diameter of 64 mm at a weight of about 280 g. A hollow flow tube with quasi-elliptical cross-section of 40 mm × 30 mm diameter extends along the longitudinal axis of the UCASS, through which the sample air flows and in which the particles are detected. Particle detection with UCASS is carried out by optical detection of the scattered light caused by particles upon crossing a diode-emitted laser beam. The optical system of the UCASS defines a particle detection region of 0.5 mm^2 in size (Girdwood, 2023). In Fig. 1, the principal setup of the UCASS instrument is illustrated, for more details see Smith et al. (2019), Girdwood et al. (2022), or Girdwood (2023).

Particles are counted, which pass through the instrument's optically sensitive region along the detection laser. The ratio of the scattered light generated by a penetrating particle is determined by means of two annular elements in the detector optics. This signal ratio is judged according to whether a detection event contributes an accepted count value or not. Based on scattered light intensity, the accepted counts are categorised into size classes (16 bins) using size-based look-up tables obtained by calibrations and based on Mie theory. Depending on the chemical composition of detected particles, different refractive indices must be considered, for example between 1.31+0j (water) and 1.52+0.002j (Saharan dust) (see Girdwood (2023) for further, more specific details) whilst for Saharan dust also other values are found, e.g. 1.53−0.0015j (Kandler et al., 2007). Knowledge of the flow velocity and the dimensions of the sensing volume is required to determining accurate particle concentrations.

3.2 The thermal flow sensor (TFS)

The thermal flow sensor (TFS) model "FLW-122" for the gaseous media by B+B Thermo-Technik GmbH was used for this study. The TFS has a length of 6.9 mm, is 2.4 mm wide, and 0.2 mm high (without electrical connections). The TFS surface consists of two platinum resistor elements, one of which is the heater and the other is the reference element. The heater is a small-sized low-resistance element ($R_{\mathrm{H}}(0\ °C) = 45\ \Omega$), the reference element ($R_{\mathrm{S}}(0\ °C) = 1200\ \Omega$) is of high electrical resistance. The two platinum resistors are interconnected and are adjusted via applied voltage to a specified temperature difference. The heat dissipation from the heater to the environment corresponds to the energy loss per unit of time, which in turn corresponds to the power P converted in the resistor.

The temperature of the heating resistor decreases with increasing rate of flow surrounding the TFS. As platinum is a PTC thermistor, the conductivity of the resistor increases as the temperature falls, hence the resistance of the heater decreases. To counteract this and to maintain the differential temperature between heater and reference, the voltage is increased. The higher the flow velocity, the higher is the voltage (hereafter: signal voltage) required to maintain temperature difference. According to the sensor data sheet (B+B-Thermo-Technik, 2016), the sensor's response sensitivity is 0.01 m s^{-1} with an accuracy of better than 3 % and a temperature sensitivity of usually less than 0.1 % K^{-1}. The raw TFS data is recorded with a resolution of at least 4 Hz and then averaged to the common 1 Hz data basis. Thus, most important variabilities in the UCASS-internal flow should be captured in sufficient resolution. In addition, low-frequency influences such as the pendulum motion (order of magnitude 0.1 Hz) and the rotation (of 1 Hz at most) of the balloon payload are also temporally resolved. Further detailed information on the TFS (e.g. concerning power and sensitivity of the implemented Z-diode) may be found in the manufacturer's manual (B+B-Thermo-Technik, 2016).

For TFS calibrations, the following parameterisation, a modified form of King's law (Guellouz and Tavoularis, 1995), is often used:

$$U^2 = A + B \cdot v_{\mathrm{TFS}}^N , \qquad\qquad 1$$

where A (in V^2), B (in V^2 s m^{-1}), and N (dimensionless) are coefficients determined by calibrations, v_{TFS} is the flow velocity (in m s^{-1}) and U is the electrical output voltage (V). Rearrangement of Eq. 1 leads to the desired expression for the flow velocity (here v_{TFS}) as a function of measured voltage. King's law, a combination of Nusselt number and Reynolds number (see Cardell (1993) or Bearman (1971)), is primarily influenced by temperature fluctuations due to the temperature dependence of air's thermal conductivity and the dependence of the kinematic viscosity on the air density. Extensions of this equation by correction terms allow for considering changes of ambient temperature (see Cimbala and Park (1990)). On the one hand, these corrections apply to significantly warmer temperatures (300 – 307 K) than relevant for balloon soundings, and on the other hand require a set of temperature measurements, including the accurate temperature of the TFS surface itself. The TFS calibrations to assign a flow velocity to the output signal were carried out under laboratory conditions. To account for the dependence of the in-flight flow measurement on air density, a corresponding correction (dependent on static air pressures and ambient temperatures upon vertical sounding) is applied to measured data during post-flight analyses.

161 Based on the ideal gas law and on laboratory conditions during calibrations (p_0, T_0, and humidity
162 expressed as virtual temperature), the correction $v_{\text{TFS}}^{\text{corr}}$ is obtained by multiplying v_{TFS} (according
163 to Eq. 1) with a correction factor (at given ambient conditions p_{amb}, T_{amb}):

$$v_{\text{TFS}}^{\text{corr}} = v_{\text{TFS}} \frac{p_0}{p_{\text{amb}}} \cdot \frac{T_{\text{vi}}}{T_0} \qquad\qquad 2$$

164

165 The virtual temperature T_{vi} was used instead of the ambient temperature T_{amb}. Hence, any change
166 in air's molar weight, air's mass density, and heat capacity due to water vapor load is accounted
167 for. As long as no phase conversion occurs the temperature ratio also reflects the current moisture
168 conditions in the atmosphere.

169 In addition, a cold chamber test was carried out at various temperatures down to – 20°C
170 (electronic supplement, S1) to investigate the sensitivity of the TFS system (particularly its
171 electronic compounds) to significantly colder temperatures than those under laboratory
172 conditions.

173 To mount the TFS on the UCASS, a 3D-printed polylactide case was produced. This was precisely
174 adapted to the dimensions of the inner flow tube and the outer shape of the UCASS and extends
175 the total length of the UCASS by a further 49 mm (cf. Fig. 2).

3.3 The Prandtl-Pitot tube
177 The Prandtl-Pitot tube (PPt) model "TSI 8710 plus" (re-calibrated in July 2022 for flow velocities
178 of 1 – 10 m s^{-1}) by TSI Inc. was used as reference instrument for calibrating the TFS. Via the pitot
179 tube's entry, aligned against the direction of flow, the stagnation pressure (the sum of the dynamic
180 and static pressure components) is measured. The outer tube of the Prandtl-instrument with
181 ring-shaped perforation, allows for measuring the static pressure component. Conversion of
182 Bernoulli's theorem to resolve to the flow velocity, leads to:

$$v_{\text{PPt}} = \sqrt{\frac{2\left(p - p_{\text{stat}}\right)}{\rho}} \; , \qquad\qquad \mathbf{3}$$

183

184 where p_{stat} is the static pressure (in hPa), ρ is air's mass density (in kg m^{-3}), v_{PPt} is the flow velocity
185 (in m s^{-1}), and p is the stagnation pressure (in hPa). According to the PPt's calibration certificate
186 an uncertainty of generally less than 1.5 % (at 1 m s^{-1}) is to be expected, which decreases to
187 ~ 0.6 % at a flow velocity of 10 m s^{-1}.

3.4 The wind tunnel
189 The calibrations have been conducted in the horizontal wind tunnel of the JGU Mainz. This facility
190 (schematic in the electronic supplement, Fig. S 3) has a total length of 4.6 m and a circular outlet
191 opening of 0.64 m. The maximum achievable wind speed is approximately 20 m s^{-1} generated by
192 a 12-bladed impeller rotor in combination with a 14-bladed stator, both of which have an outer
193 diameter of 0.8 m. The rotor hub (0.4 m in diameter) is encased by a tapered cone downstream of
194 the stator to aerodynamically optimise the transition from the impeller housing (total length
195 1.25 m) to the flow channel (3.41 m length). The flow channel widens at 7° towards the horizontal
196 over a horizontal distance of ~ 2.0 m. In the area of the maximum channel diameter, a gauze, and
197 a honeycomb mesh with a total thickness of 0.1 m are installed to laminarise the flow. Further
198 downstream, the flow channel diameter reduces via a radiused narrowing to compress the air
199 flow. The channel's outlet with a constant diameter of 0.64 m extends over a distance of 0.35 m.

3.5 Calibration setup and procedures

Generally, all setups for the TFS calibration were placed centrally within the wind tunnel's laminar exit flow and in line with the tunnel's ring outlet edge to prevent potentially forming turbulence from affecting the calibration.

3.5.1 TFS – PPt interactions

For exploring whether an extension of the UCASS by the TFS housing (with installed TFS) causes a measurable impact on the flow at the position of the UCASS optical detection region, a 3D-printed replica of the UCASS housing was used. Holes were drilled into the housing replica at two different positions along its longitudinal axis in order to 1) place the PPt inlet at the position of the optical detection area within the flow tube and 2) place the PPt inlet inside the TFS housing at the TFS's position while replacing the TFS. The replica housing was lacking all optical elements (laser diode, mirrors or photodiodes) that an operational UCASS comprises; all bulges along the flow tube's inner wall were evened out for this experiment.

Furthermore, a thermal anemometer (TA, by TSI Inc., model TSI 8455-300-1) was used to control the ambient flow generated by the wind tunnel. The TA was calibrated against the PPt in the free tunnel flow at flow velocities of 2 – 8 m s^{-1}. Then the experimental setup of the UCASS replica with integrated PPt was aligned iso-axially in the central flow of the wind tunnel. The experiments carried out are listed in Table 1.

The experiments were conducted at ambient wind tunnel air flows of $2 \leq v < 10$ m s^{-1} in increments of ~ 1 m s^{-1}. 10 individual measurements were averaged for each of the seven different wind speeds. The result of this experiments is shown in Fig. S 4 as correlations between TA-measured flow speeds (v_{TA}) against those from the PPt (v_{PPt}) within the UCASS flow tube. Notably, the UCASS tube flow velocity was generally increased compared to ambient wind speeds if the UCASS is iso-axially aligned with the ambient flow field, which was previously described by Smith et al. (2019) and confirmed during calibrations presented herein (see Sect. 4.2).

This experiment series demonstrate that applied modifications (extension of the flow tube geometry and implementation of the TFS) have hardly any measurable influence on the flow through a UCASS. At balloon ascent velocities, usually well below 10 m s^{-1}, none of the data series stood out from the statistical uncertainty. Therefore, the technical modification proposed herein is expected to have negligible impact on the measurement performance of the UCASS.

3.5.2 Cross sectional flow profile

For the following, a TFS housing shell without installed TFS was mounted on a UCASS to exclude any obstacle for the air stream through the flow tube. The PPt was attached near the outlet of the TFS housing so that the PPt inlet was iso-axially aligned and positioned as far as possible inside the flow tube along the longitudinal axis of the UCASS. Thus, along the setup's longitudinal axis, the PPt inlet was located at the point where the TFS would normally reside. The PPt was moved perpendicularly to the flow and in small increments (~1-2 mm) along a line between the two extremes of the flow tube's elliptical cross-section. The flow speed in the wind tunnel was kept constant, and for a single data point the average of 15 velocity measurements was taken at each PPt position. The profile measurements of the tube flow profile were carried out for a tunnel wind speed of about 5 m s^{-1} and 7 m s^{-1}.

Figure 3 shows corresponding results. The maximum standard deviation in PPt's position is estimated to be 0.2 mm and is shown together with the maximum standard deviation of the PPt

243 data obtained from this series of measurements (σ_{max} = 0.05 m s^{-1}) in the bold-framed box. The
244 position where the TFS would be aligned (if - except for this experiment – installed and adjusted
245 by means of a positioning device) is marked by the grey-shaded area in Fig. 3. The flow profiles
246 exhibit asymmetry. The boundary layer at the positive end of the y-axis seems broader than at its
247 negative end. The reason for this is most likely the quasi-elliptic but asymmetric flow tube cross
248 section of the UCASS flow tube. As the ambient flow increases, an increased boundary layer
249 thickness is visible in the UCASS internal flow profile. Moreover, the flattening of the flow profile
250 is clearly visible towards the centre of the flow tube. For typical UCASS flow rates (here ~ 2-
251 10 m s^{-1}) this demonstrates, that at intended installation position (grey shaded area), the TFS
252 flow measurement occurs in the free tube flow of the UCASS. Notably, the determined cross-
253 sectional profile applies to a straight-line flow (i.e. the AOA equals zero). Under variable AOA (see
254 Sect. 3.5.4) and at the selected TFS position any wall effects still have the least influence on the
255 TFS measurement compared to other positions along the tube's cross-section.

3.5.3 Iso-axial flow calibrations

257 With the iso-axially aligned setup (see beginning of Sect. 3.5) and with the PPt inserted from the
258 rear into the UCASS/TFS housing, such that the PPt inlet is positioned close to the TFS (cf. 3.5.2
259 and Fig. 2b), the flow calibrations were performed. The TA installed in the free wind tunnel flow
260 (outside the UCASS housing, see 3.5.1) was used to control the ambient flow speed.

261 The TFS calibration comprised a series of measurements at different flow velocities. From slightly
262 more than 0 m s^{-1} stepwise increasing flow velocities were set in the wind tunnel until ~ 10 m s^{-1}
263 was reached. About 25 measured values were recorded for the calibration of a single TFS. As
264 disturbance-related fluctuations occurred in the measured values during the calibration of both
265 the PPt and the TFS, 15 measured values were recorded for each of the sensors at each ambient
266 flow speed set. Mean values and standard deviations were determined from these PPt and TFS
267 data. Each TFS was calibrated individually, and the results of these calibration series are
268 summarised in Sect. 4.1 ff. After changing the TFS, the iso-axial and centred alignment of the
269 experiment setup at the wind tunnel outlet was frequently checked and readjusted if necessary.

3.5.4 Flow calibrations under variable AOA

271 For balloon soundings, the payload (incl. UCASS) is usually attached approx. 60 metres (via
272 unwinder, model "UW1" by Graw GmbH & Co. KG) below the balloon on a cord. The long cord is
273 intended to dampen the pendulum motion of the payload. Due to the vertical offset between the
274 balloon and the payload, also a horizontal offset between both ballon and payload occurs
275 depending on the horizontal wind speed. The balloon may lead the payload by a certain horizontal
276 distance, unless the horizontal wind speed is zero. Hence, during the balloon's ascent and with
277 horizontal winds the UCASS is likely inclined at a certain angle relative to the direction of vertical
278 lift. In addition, pendulum motion and rotations of the payload during flight cannot be completely
279 prevented, which can lead to a variable alignment of the UCASS relative to a straight ascent due
280 to several superimposed effects. Therefore, the impact of inclinations of the UCASS with respect
281 to the direction of flow on 1) the TFS calibration and 2) on the flow velocity within the UCASS is
282 to be quantified.

283 The experimental setup was aligned and positioned as described previously (beginning of Sect.
284 3.5). The iso-axial alignment corresponds to the zero position (φ = 0°, ϑ = 0°). As the UCASS flow
285 tube is mirror-symmetrical along the vertical axis, the UCASS was horizontally inclined only along
286 the positive x-axis (φ) for changing AOA. Due to the quasi-elliptical shape of the UCASS flow tube,

287 the effects of the flow angle in y-direction (ϑ) were analysed for both the positive (UCASS inlet
288 points upwards) and the negative (UCASS inlet points downwards) deviation from zero. Figure 4
289 illustrates the measurement setup and provides an example of the angular distribution under
290 which the UCASS was aligned relative to the ambient flow field. Note, that the frame for holding
291 the UCASS/TFS setup also fixes the PPt (marked in Fig. 4a), which remains aligned with the UCASS
292 longitudinal axis and is positioned as close as possible at the TFS. Any angular change in the flow
293 direction to the UCASS inlet therefore affects the entire assembly (cf. Fig. 4c). At the beginning of
294 each measurement series, data were recorded for five different ambient flow speeds in the zero
295 position (0°, 0°) to verify the calibration curve of respective TFS used. The angles were then set
296 within the angle grid shown in Fig. 4b. 15 measured values of the PPt and the TFS were recorded
297 for five different tunnel flow speeds between about 3 and 7 m s^{-1} and the mean value with
298 standard deviation were determined from PPt and TFS data. The results are summarised in Sect.
299 4.3. An attempt was made to reproduce the set tunnel flow velocities for each measurement series
300 at varied AOA, which allowed also for investigating the relationship between the flow velocities
301 outside and inside the UCASS housing at variable AOA (see Sect. 4.4).

3.6 UCASS internal flow estimates

303 Besides the counted and classified particles, UCASS also records the particles' average beam
304 transit times (named MToF, Mean Time of Flight) in four different size ranges. In principle, these
305 beam transit times could be used to estimate the flow speed in the measurement volume and
306 therefore would provide another option for a sampling volume assessment. Such an approach is
307 used for example in connection with the particle detectors by Alphasense OPC-N2 and OPC-N3
308 (Bezantakos et al., 2020). We therefore correlated the measured TFS velocities with the inverse
309 of the different MToF values reported for each interval, when particles were detected. A
310 considerable number of apparently clipped values (piling at the apparent bottom and top end of
311 the measurement scale) were removed. Still, while there was a very weak correlation found
312 between the inverse MToF and the TFS, the huge variations, the clipped values and the scarcity of
313 data - in most 0.5 second intervals no particles are detected - prevent this approach from being
314 used as a measurement for a flow rate in UCASS.

4 Calibration results

316 To this point, it has been demonstrated that

317   1) the insertion of the TFS into the flow tube of the UCASS has no measurable impact on its
318   particle-sensitive area (Sect. 3.5.1) and
319   2) as the TFS installation is achieved by using a positioning device it is systematic for all TFSs
320   used whose measurements occur outside the tube's boundary layer in the central UCASS
321   flow.

322 Hence, the assumption seems appropriate that integrating TFS into the UCASS flow tube did not
323 generate any additional interferences for the calibrations discussed hereinafter.

4.1 High resolution (HRC) and three-point calibration (TPC) of the TFS

325 According to the functional relationship described in Eq. 1 the measured TFS output voltage is
326 calibrated versus the PPt-measured flow velocity, which is used hereafter as the calibration curve
327 of a TFS (further details in Sect. S 2 in the electronic supplement). For each measuring point, the
328 mean value plus (minus) the associated standard deviation - i.e. the extremes of variability - was

329 inserted into the calibration curve function yielding a deviation from the averaged measurement
330 point by not more than 0.08 m s^{-1} corresponding to a percentage maximum of 1.3 %. The results
331 show that the different TFS exhibit very similar behaviour and that the parameterisation of the
332 calibration curve function is valid for all calibrated TFS. Table S 1 (see electronic supplement)
333 lists the parameterisation coefficients for the TFS analysed in the calibration results. Repeated
334 calibration series with a larger time offset and with the same TFS after disassembly/reassembly
335 of the setup also reproduced previous values within 1.8 % at maximum, and on average within
336 1 %, in the relevant range of ambient flows. However, the measurements of the calibration curves
337 were likely influenced by the ambient temperature and pressure conditions in the laboratory as
338 both affect air's mass density, which in turn controls the heat advection at the TFS.

339 In the process of these high-resolution calibrations (calibrations with up to 25 data points and in
340 the following denoted as HRC) and analyses of the calibration curves, it was found that only three
341 calibration points (at ~2, 5, 8 m s^{-1}) reproduce the calibration curve with acceptable accuracy
342 (see electronic supplement, Sect. S 2, for details). For the TFS used (here: TFS 8), and at tunnel
343 flow speeds between 2 and 8 m s^{-1}, the three-point calibration (in the following denoted as TPC)
344 curves did not deviate by more than 1 % from the highly resolved initial calibration curve.

4.2 Internal versus external flow velocity

346 The PPt was repositioned next to and slightly upstream of the UCASS inlet to measure in the free
347 flow of the wind tunnel (setup is shown in Fig. S 5). The UCASS-integrated TFS 8 had previously
348 been calibrated with the PPt to have a calibration curve (TFS 8.2 (TPC) see Table S1) under the
349 same laboratory conditions as the experiment. The UCASS was aligned iso-axially to the ambient
350 flow of the wind tunnel and centred at the annular outlet of the tunnel. The wind tunnel flows
351 were stepwise increased from slightly more than 0 to up to 11 m s^{-1} and then decreased with a
352 total of 17 different settings. For each of the ambient flow speeds, 15 velocity values were
353 recorded as measured by the PPt to be averaged. In Fig. S 6, the PPt-measured flow velocity
354 outside the UCASS is displayed in reference to the UCASS internal flow velocity determined with
355 the TFS 8. The velocity range relevant for balloon soundings (2 - 8 m s^{-1}) is indicated by the black
356 dashed square.

357 Within this range, 10 different values of ambient flow speed were set for each measurement of
358 this series. The standard deviation σ of the PPt data range between 0.01 and 0.04 m s^{-1}. Only the
359 mean value of the TFS output voltage was noted, which resulted from the automated averaging
360 by the multimeter used. During the TFS 8 calibrations, standard deviations of at the most 0.08 m s^{-1}
361 $^{-1}$ were obtained corresponding to a maximum relative deviation of 1.3 % (extremes of variability,
362 cf. first paragraph in Sect. 4.1). A first-order polynomial fit was created for the recorded
363 measurement. The resulting line-fit indicates that in an iso-axial arrangement the UCASS internal
364 flow velocity exceeds the outside flow speed. Calculated from 10 data points at external wind
365 velocities between 2 and 8 m s^{-1}, the UCASS internal flow velocity is increased by 10.7 to 11.9 %,
366 with an average relative deviation of 11.3 %, as compared to the external flow speed.

367 This result quantitatively compares well with the results of Smith et al. (2019), who simulated an
368 increase in the UCASS internal flow velocity by 12 % under an iso-axial alignment of the UCASS
369 and at an ambient flow speed of 5 m s^{-1}. Taking into account the standard deviations of averaged
370 data points determined here may put the small deviation between previous and current results
371 into perspective.

372 However, in balloon-borne UCASS field applications, the balloon ascent rate is usually used to
373 determine the sample volume flow and thus the measured particle number concentrations (e.g.
374 Kezoudi et al. (2021)). So, when a UCASS was iso-axially aligned during a straight balloon ascent
375 at rates of 2 to 8 m s^{-1}, the GPS or pressure-based calculation would lead to an underestimated
376 UCASS sample volume flow by about 11-12 % and the particle number concentrations would be
377 overestimated accordingly. Therefore, from current point, a direct measurement of the UCASS
378 internal flow velocity during flight appears useful, but as will be shown (Sect. 5), the conditions
379 during balloon soundings are more complex and the necessity for a flow velocity detector
380 integrated into the UCASS gets all the more obvious.

4.3 UCASS internal flow velocity under variable AOA

382 Compared to previous experiment series, the UCASS was intentionally misaligned from the iso-
383 axial orientation (cf. Sect. 3.5.4).

384 Figure 5 shows the highly resolved calibration curve TFS 8. The mean values from experiment
385 series at five ambient flow speeds are also depicted for each AOA. The standard deviations are not
386 shown for the sake of clarity of the figure. The error in setting the UCASS deflection angle was
387 estimated to be ±0.5° in each case. In the zero position (0°, 0°), which was calibrated once at the
388 beginning and at the end of the series, the σ-values ranged between 0.002 and 0.003 V (TFS 8
389 output voltage) or between 0.02 and 0.04 m s^{-1} (PPt). With increasing AOA, the standard
390 deviations (σ) rose to a maximum of 0.025 V (TFS 8) and 0.09 m s^{-1} (PPt). Hence, the fluctuations
391 of measured variables generally increased with increasing AOA.

392 Based on the TFS 8 calibration curve, the flow velocities $v_{\mathrm{TFS}}^{a}(U)$ were determined with the mean
393 TFS output voltage values ($\overline{U}$). These are compared with the flow velocities $v_{\mathrm{TFS}}^{b}(U)$ resulting
394 from the extreme values of standard deviation at each mean output voltage (i.e. $\overline{U} \pm \sigma$). The
395 maximum standard deviation range observed was ± 0.31 m s^{-1} (8.3 %). Oscilloscope records of
396 the variations in the TFS output voltage over 20 s clearly indicated an increasing scatter intensity
397 when varying the AOA of UCASS, e.g. from (0°, 0°) to (20°, -40°). The output voltage fluctuations
398 were invariant in time (in particular non-periodic) and stationary, i.e. rather of a statistical nature.

399 The mean values of the TFS measurements were inserted into the calibration curve function of
400 TFS 8 to determine the flow velocities (v_{TFS}) to be juxtaposed to the mean PPt-measured flow
401 velocities (v_{PPt}). The flow velocity determined with the calibration curve was used as the reference
402 and an error is considered with

403 $$\varepsilon = \frac{v_{\mathrm{TFS}} - v_{\mathrm{PPt}}}{v_{\mathrm{TFS}}} \cdot 100, \qquad\qquad 4$$

404 out of which the maximum percentage error and its mean resulted for each AOA. Table 3 shows
405 the maximum and the mean of the relative percentage deviation of measured values at variable
406 AOA compared to the calibration curve TFS 8. At AOA of up to 30°, the maximum relative
407 percentage deviation was 3.5 %, and above 30°, the relative percentage deviation of measured
408 values from the calibration curve increased significantly. At such large AOA, the σ of TFS-
409 measured voltages also rose substantially. During balloon sounding, UCASS inclinations of more
410 than 30° from the vertical are not expected. In an earlier study (Smith et al., 2019), a model was
411 used to simulate the angular inclination of the UCASS in relationship to the direction of ascent.
412 Initial pendulum oscillations of up to ± 20° were assumed, which were damped to around ± 5°
413 within about 30 seconds. If these conditions occurred at an actual balloon sounding with UCASS,
414 the percentage relative deviation of measured velocities as determined here (based on the TSF 8

calibration curve) would be a maximum of 2.8 % under variable AOA smaller than 20°. Hence, even at UCASS inclinations of up to 20°, the particle concentration is affected by this angle deflection with a maximum uncertainty of less than 3 % (maximum relative deviation). To validate the TFS 8 data series, the measurements were repeated with TFS 7 in the same setup. Corresponding results are summarised in Sect. S 3 (electronic supplement) representing a qualitative and largely quantitative confirmation of the results and conclusions made.

4.4 Internal versus external flow velocity under variable AOA

In Fig. 6, the velocity of TA-measured ambient wind tunnel flows (as reference) is plotted against the PPt-measured flow velocity inside UCASS. Standard deviations of 0.01 to 0.10 m s^{-1} were determined for the ambient flow velocity between 2 and 8 m s^{-1}. For PPt data, σ-values ranged from 0.02 to 0.09 m s^{-1}, which increased with rising ambient flow velocities and AOA. With increasing AOA, the UCASS-internal flow velocity decreased. For AOA of (0°, 30°) and (0°, -30°), and beyond, the UCASS-internal flow was slower compared to external flow velocities.

The UCASS-internal flows in zero-position (0°, 0°) were used as reference and parameterised by a first-order polynomial fit. The comparison of a) the calculated flow velocity inside the iso-axially aligned UCASS with b) its internal flow velocities at AOA of (0°, 30°) and (0°, -30°) revealed a relative percentage decrease in the flow velocity of around 15 % (see Table 4). For an iso-axially aligned UCASS, the internal flow is accelerated by on average ~ 11.3 % (see Sect. 4.2). The contrary effects of a) a flow acceleration inside the iso-axially aligned UCASS and b) the deceleration inside the UCASS when deflected from the zero-position are likely superimposed. Thus, with a UCASS inclination of 30° during a balloon sounding, the internal UCASS flow velocity is reduced by around 4 % net compared to the external flow. In turn, at such UCASS inclination, a particle number concentration calculated with the GPS or pressure-based ascent velocities underestimates the prevailing trace material concentrations by only about 4 % under these conditions.

At a certain deflection angle (30°, 0°) a noticeable but undeterminable interference effect appears to have impacted the laboratory experiments. With increased deflection of the UCASS, the inlet opening of the UCASS is shifted out of the central wind tunnel flow and towards the tunnel's wall. With decreasing distance to the wall of the wind tunnel, effects of flow disturbances cannot be ruled out, which could influence the relative deviation from the calibration curve. Potentially, signal fluctuations are also amplified by flow disturbances that occur at the leading edge of the UCASS entrance when the UCASS is deflected too far from the zero-position. The TFS appears to be sensitive to such fluctuations. In addition, an influence of wind gusts on the experiment cannot be excluded, as the wind tunnel is operated inside a building, but has connections to the building's exterior to enable enhanced wind tunnel flows.

5 Ambient measurements

Ambient balloon soundings were carried out with two UCASS instruments, such that two TFS were operated in parallel during respective ascent. The balloons' ascent rate is determined from both the static pressure measurement (v_{p}) and the GPS data, each of which is recorded independently. The static pressure in flight, resolved at 1 Hz, is converted to barometric altitudes by the internal primary data processing in the VAISALA sounding system, as recalculations (based on Sonntag (1994)) confirm. GPS and pressure-derived ascent rates correlate very well

457   (regression yields a slope of one and a constant element of - 0.1 m s^{-1} with a coefficient of
458   determination r^2 of 0.99).

5.1 Vertical profiles

460   Figure 7 shows vertical profiles of three balloon soundings launched from Tailfingen (Germany),
461   at ~ 900 m above sea level (a.s.l.) in August 2023. The profiles allow for comparing 1) the balloon
462   ascent rate from the GPS measurements v_{GPS}, 2) the balloon ascent velocity from the static
463   pressure measurements v_p, and 3) the flow velocities through the two UCASS units (TFS 1 and
464   TFS 2) operated on each ascent. Results from other balloon soundings are shown in the electronic
465   supplement (Fig. S 10). The TFS used for the balloon soundings and their calibration coefficients
466   are listed in Table S3. The profiles are limited to an altitude of 7.5 km a.s.l., as at about this height
467   the ambient temperatures fell below the specified temperature limit (253 K, see B+B-Thermo-
468   Technik (2016)). Further laboratory tests are required to confirm the robustness of the TFS
469   measurements also at temperatures of 253 - 220 K or to reveal the need of further corrections. As
470   nearly all UCASS particle measurements were detected below 7.5 km, the restricted height range
471   nevertheless covers the relevant part of the flight. The data are low-pass filtered by a 10-second
472   running average.

473   A common feature of the vertical profiles is the stronger scatter of the GPS-derived ascent rates
474   compared to those based on pressure measurements. This might be connected to a larger
475   uncertainty inherent with the GPS. In general, however, both values are well-correlated. Up to
476   ~ 2 km of the balloon sounding of 12 August (Fig. 7a) the TFS measurements agree relatively well
477   with GPS and the pressure data (see also Fig. 7b). Below ~ 3 km, TFS 1 and TFS 2 deviate from the
478   pressure and GPS data by up to 30 %. Up to ~ 3.8 km, the different speed measurements from all
479   instruments are comparatively consistent. Above 3.8 km, the TFS measurements (again consistent
480   between TFS 1 and 2) show periodically fluctuating and lower flow speeds (by up to 15 %, and
481   above 7 km altitude by up to 25 %) compared to those resulting from GPS and pressure.

482   During the earlier balloon sounding of 16 August (Fig. 7d) and up to an altitude of ~ 2.4 km, the
483   TFS-based velocities are systematically higher (in peaks by up to 45 %, cf. Fig. 7e) than
484   corresponding values from GPS and pressure. In contrast to the previous case, the measurements
485   of the four sensors are quite consistent at altitudes between 2.4 and 5.3 km with deviations of
486   seldomly more than ± 10 %. Above ~ 5.3 km, the two independent TFS measurements, which
487   correlate quite well with each other, both deviate increasingly from the GPS and barometric data
488   with increasing altitude and show up to 15 % lower UCASS flows compared to the balloon ascent
489   rates.

490   The balloon sounding on the afternoon of 16 August (Fig. 7g) shows a more or less satisfactory
491   match between all four independent measurements only at the lowest altitudes (up to ~ 1.3 km).
492   Between 1.3 and 2.7 km, the TFS- velocities are generally higher (on average by 15 %, in peaks up
493   to 25 %, cf. Fig. 7h) than those derived from GPS and pressure. Above 3.2 km, reversely the ascent
494   velocities from pressure and GPS slightly exceed the TFS data. At altitudes of 4.5-5.5 km and above
495   ~ 6.2 km, GPS and pressure measurements commonly reveal increased vertical velocities that
496   rise from about 6 m s^{-1} to about 8 m s^{-1}. Within these layers TFS-velocities are mostly 15 % (in
497   peaks up to 25 %) slower than the ambient air flow. The origin of these features in the GPS and
498   pressure-based velocity profile apparently has, if any, only minor impact on the TFS
499   measurements.

500 These examples suggest that over large parts of the vertical sounding (up to 7.5 km altitude) the
501 flow velocity within the UCASS (and thus through its optically sensitive particle detection region)
502 does not match the GPS or p-derived ambient flow velocity. For each of the vertical soundings
503 shown in Fig. 7, the speeds of the horizontal wind components (u and v) and the sum of both as
504 total wind speed are also displayed in vertical profiles (Fig. 7 c, f, i). Occasionally, changing wind
505 speeds appear to be reflected in changing velocity ratios (e.g., the decrease in u at 4 km and 6 km
506 in Fig. 7c or the features in u at 5 km in Fig. 7f and at ~ 6 km in Fig. 7i), which would indicate a
507 certain correlation. However, a general causality between changing wind speeds and the ratio of
508 TFS-based to p-based flow velocities through the UCASS cannot be inferred without knowledge of
509 the actually resulting AOA at which the UCASS are sampling. Besides wind speeds, also stability
510 (Brunt-Väisälä frequency N^2), turbulence (Richardson number, Ri), and wind shear as function of
511 altitude (not shown herein) were investigated concerning their potential relationship with the
512 variable velocity ratios, but none of general validity could be identified.

5.2 Implications of observed features

514 Influences on the UCASS-internal flow speed and pattern due to an additional installation of a TFS
515 in a housing extension, if any, are negligible (Sect. 3.5.1). The sensitive area of the implemented
516 TFS is located within the free tube flow through a UCASS, i.e. outside the boundary layer of the
517 UCASS flow tube's inner walls (Sect. 3.5.2). Moreover, with an iso-axial alignment of the UCASS,
518 the inner flow is accelerated by ~ 11.3 % when compared to the ambient flow velocity around the
519 UCASS (Sect. 4.2), which is in general agreement with earlier findings (Smith et al., 2019). As
520 discussed in Sect. 4.4, with increasing angular deflection of the UCASS from the iso-axial
521 orientation, the flow velocity inside a UCASS is decelerated towards values of the ambient flow
522 speed and below.

523 The payload as used during the field mission had a total weight of up to 3.9 kg. About 10,000 litres
524 of helium are required for the balloon to yield enough buoyancy for desired lift. Under conditions
525 with horizontal winds, the effective surface area of the filled balloon is many times larger than
526 that of the payload structure (<0.1 m^3). When fully unwound, the flexible cord between the
527 balloon hull and the payload extends up to ~ 60 m. During its ascent from the ground through the
528 boundary layer, the balloon hull (with a larger surface area compared to other components of the
529 balloon assembly, which is moreover located several dozen meters above the payload) is
530 frequently exposed to varying wind speeds (cf. Fig. 7). With increasing altitude and decreasing
531 ground friction, the (variable) wind shear increases equally. Therefore, during its ascent, the
532 balloon assembly generally tilts relative to the vertical as soon as horizontal wind speeds other
533 than zero prevail, as shown by the horizontal displacement between two radiosondes at opposite
534 ends of a balloon payload ensemble with a total length of ~62 m (see Sect. S 4 in the electronic
535 supplement).

536 Above the boundary layer, the balloon's much larger surface area may cause it to act as a sail in
537 prevailing horizontal winds, causing the payload with a much smaller surface area to be towed
538 behind. Therefore, the balloon is most times slightly dislocated with respect to the resultant wind
539 vector compared to the payload, the payload will inevitably be inclined relative to the wind vector
540 over large parts of the balloon sounding.

541 Based on the ratios of the TFS measurements compared to the ascent velocities from GPS and
542 pressure measurements, different scenarios arise over a flight, in which

1. The flow velocities through the UCASS are increased compared to the ascent velocities: as if the deflection angle of the UCASS relative to the vertical was comparatively small or close to an iso-axial alignment of the UCASS within the ambient flow,

2. The flow velocities through the UCASS are within the variability range of the GPS and pressure measurements of the ascent velocities: for this, a deflection of the UCASS of about 20°-30° would have to be attained (cf. Fig. 6 and Table 2) while an enhanced uncertainty is hereby accounted for by using the TA instead of the PPt for measuring the wind tunnel flow speed, as the PPt measured at that time inside the UCASS housing,

3. A flow velocity through the UCASS that is smaller than the GPS or pressure-based ascent velocities: for this, a deflection of the UCASS of about >30° would have to be reached.

For the last of these points in particular, the required deflection angles of the UCASS appear extreme to clearly explain observed velocity ratios. In addition, pendulum movements of the payload around a position in the inclined state (i.e. without swinging through the pendulum's equilibrium, which would correspond to an iso-axial, strictly vertical UCASS alignment) could generate a continuously variable orientation of the UCASS in the flow. Moreover, it was observed that the payload can rotate around its vertical axis (in line with the balloon cord). The superposition of these movements and others resulting from the variability of the payload's lift (e.g. indicated by fluctuations in GPS and pressure-based ascent rates) may lead to various influences on the flow through the UCASS, which currently are neither separable nor quantifiable. As the ascent speed is mainly determined by the balloon's buoyancy, drag force, and gravitation, the resulting wind situation at the payload may differ from that at the balloon due to small scale atmospheric variability (e.g. turbulence).

During balloon soundings, the flow velocity through the UCASS is subject to complex influences and is largely decoupled from the pure vertical velocity (i.e. the ascent rate) of the balloon. The high variability of the flow velocity measured during ascent directly inside the UCASS emphasises the importance of such a direct measurement. The frequent deviation of the UCASS flow speed from the GPS or pressure-based vertical velocity is one further argument in favour of implementing an independent flow sensor inside the UCASS. The GPS or pressure-based ascent rates deviate by values in the range of metres per second from the UCASS internal flow velocity. Based on a velocity of 6 m s^{-1}, a deviation by ± 0.5-2 m s^{-1} results in an error of ± 10-30 % and a corresponding over- or underestimation of the resulting particle number concentration.

Table 5 summarises the main uncertainties arising from the different methods for determining a flow velocity through UCASS and which have equal quantitative impact on resulting particle number concentrations. From the Gaussian error propagation of the relationship given in Eq. 1 and Eq. 2 an overall uncertainty $\Delta v_{\mathrm{TFS}}^{\mathrm{corr}}$ combines from 1) the uncertainties in T and p measured with a radiosonde RS 41 SGP (Vaisala, 2024) also including uncertainties arising from the TFS calibrations conditions (in p_0 and T_0) and 2) the uncertainty Δv_{TFS} (i.e. determined σ) obtained from the cold chamber test at different ambient temperature conditions (cf. Sect. S 1 in the electronic supplement). For three chosen temperatures (i.e. 275 K, 264 K, and 254 K) from these chamber experiments the corresponding deviations of the GPS-based flow velocities (Δv_{GPS}) from corresponding $v_{\mathrm{TFS}}^{\mathrm{corr}}$ are determined at equal temperature conditions during three vertical soundings (Fig. 7 and adjacent text). Thus, the total uncertainty in $v_{\mathrm{TFS}}^{\mathrm{corr}}$ is fairly consistent within a range between 6.9 % and 8.8 % (values asterisked in Table 5). In a few of the conditions selected here (275 K and 264 K), resulting Δv_{GPS} is comparatively low (values framed between two vertical lines in Table 5), or in almost similar range of $\Delta v_{\mathrm{TFS}}^{\mathrm{corr}}$ (values framed between two horizontal

588   lines) however, in other cases (enclosed framed values) the offset in v_{GPS} is significant and can
589   exceed 30 % (occasionally even more as seen in Fig. 7d). In essence, v_{GPS} appears as the more
590   precise measurement, but can unpredictably become highly inaccurate upon vertical sounding
591   over large height ranges (500 - 1500 m). In contrast, v_{TFS}^{corr} presumably is the more accurate
592   measurement over discussed vertical range up to ~ 7.5 km, with a comparatively higher though
593   determinable imprecision.

6 Summary and Conclusions

595   This study indicates a possible improvement of the Universal Cloud and Aerosol Sounding System
596   (UCASS), a balloon-borne optical particle counter, to obtain aerosol and cloud droplet
597   concentration measurements with increased accuracy. The integration of a thermal flow sensor
598   (TFS) into the UCASS allows for direct, real-time and continuous flow velocity measurements in
599   the immediate vicinity of UCASS's particle detection region. This approach resolves inaccuracies
600   arising from the conventional reliance on GPS or pressure-based balloon ascent velocities, which
601   do not account for gusts or strong wind shear, payload oscillations, flow distortions (caused by
602   the UCASS housing), and particularly the deflection of the UCASS body from an iso-axial alignment
603   during ascent.

604   Wind tunnel experiments showed that the UCASS-internal flow velocity, when iso-axially aligned
605   with the ambient airflow, is on average 11.3 % faster than the surrounding external flow (between
606   2 – 8 m s^{-1}), largely consistent with previous investigations. Hence, the airflow dynamics of the
607   UCASS are reproducible and predictable under controlled conditions. Further laboratory
608   experiments under variable angles-of-attack (AOA) revealed that with a deflection of the UCASS
609   by around 20° - 30°, the UCASS-internal flow velocity is reduced to values approximately
610   corresponding to the external flow velocity.

611   It was found that high-resolution calibrations of a TFS provide accurate results that are
612   parameterizable according to King's Law, with deviations of no more than 1.3 % from the mean
613   samples. A more efficiently implementable three-point calibration (TPC) method (using flow
614   velocities of approximately 2 m s^{-1}, 5 m s^{-1}, and 8 m s^{-1}) showed deviations of less than 2.9 %
615   compared to detailed calibrations.

616   During balloon soundings, UCASS-internal flow velocities could deviate significantly from the GPS
617   or pressure-based ascent rates, varying by up to 30 %. Thus, accurate measurements of particle
618   concentrations based solely on GPS or p-derived ascent rates are subject to considerable
619   uncertainty. Vertical profiles from three soundings up to 7.5 km (see Sect. 5) showed that the
620   deviations in flow velocity increased with increasing altitude due to changing atmospheric
621   conditions and balloon-payload-geometry (i.e., the inclination of the payload orientation and thus
622   the UCASS alignment). Referring to the thought model of the balloon sounding (see Sect. 2), that
623   the flight pattern of the balloon is driven by the horizontal wind components (i.e. u and $v > 0$):
624   then 1) the balloon body acts as a sail with its comparatively large surface and 2) the
625   comparatively small payload is towed. In other words, even if the main wind components with
626   respect to the payload's inertial system (u_{rel}, v_{rel}) were nearly zero, this will typically result in a
627   constellation of the balloon-payload geometry which causes a flow towards UCASS with a non-
628   zero AOA. While UCASS is aligned with the cord to the balloon, it is deflected with respect to the
629   buoyancy-induced vertical lift, i.e., iso-axial flow to the UCASS is rarely given. The actual flow,

630 which is affected by the pendulum motion and rotation of the payload and their superposition, is
631 hardly reproducible or quantifiable. This ultimately underlines the need for a continuous
632 measurement of the actual internal UCASS flow during the entire flight.

633 Hence, for airborne particle measurements the calculated particle concentrations from UCASS
634 detections based on GPS or pressure ascent rates may introduce errors of up to 30 %. Real-time
635 TFS data would reduce this uncertainty by ensuring that the actual air volume of the samples is
636 determined independently of external conditions. The integration of the TFS into the UCASS
637 therefore represents an improvement in the methodology of measuring aerosol and cloud droplet
638 concentrations up to 7.5 km. By providing direct and precise flow velocity measurements, the TFS
639 avoids the limitations of GPS or p-based methods, including errors caused by payload movements,
640 gusts, wind shear, and flow deviations caused by the shape of the UCASS housing. Field tests
641 confirmed that this approach leads to more accurate assessments of air volumes in the samples
642 and can reduce uncertainty in calculating particle number concentrations.

643 The knowledge gained may motivate future modifications and improvements in the further
644 development of the balloon-borne UCASS instrument. The robust three-point calibration methods
645 applied in this study facilitate the technical effort involved in integrating TFS into a modified
646 UCASS. This work can provide a basis for improved vertical profiling of aerosols and cloud
647 elements with cost-effective and flexible instruments such as UCASS.

648 **Code and data availability**
649 Both data and the program code are available in a repository via
650 "https://doi.org/10.5281/zenodo.15519552".

651 **Author contribution**
652 SJ performed the calibrations, reporting and optimised technical designs. SJ, RW, KK wrote the
653 article with contributions by JG, CS, WS, LKE, LV and HT. LV, LKE and CvG ensured the technical
654 operability of the TFS-equipped UCASS instruments (supported by JG, CS, WS) and the balloon
655 gondola during field missions. HT (forecasting), LKE (preparation and launch) and KK, SJ
656 (recovery) contributed invaluably to successful balloon soundings.

657 **Competing interests**
658 The authors declare that they have no conflict of interest.

659 **Acknowledgements**
660 The contributions from the technical staff at the workshops of the Institute for Physics of the
661 Atmosphere (Mainz University) and of the MPI for Chemistry were crucial and essential. In
662 particular, we acknowledge the support of H. Rott, K. Wilhelm, M. Maurer, T. Böttger, P. Schumann,
663 T. Kenntner, M Dietrich, and B. Meckel. We furthermore gratefully acknowledge the excellent
664 support by R. Dominik, I. Knapp-Wagner, J. Frielingsdorf, M. Euler, and O. Krause as well as the
665 radiomen (a. o.) W. Hallmann (DF7PN), R. Roth (DG7FDE). We are also deeply grateful for the
666 generous hospitality of M. & A. Conzelmann (Tailfingen) of A. Lampmann (BSC Spielberg), and the
667 residents of Spielberg. The authors thank the Editor C. A. Brock and two anonymous reviewers
668 for their careful evaluation of this article and their valuable and constructive recommendations.

669 **Financial support**
670 Our research was funded by the Deutsche Forschungsgemeinschaft (DFG, German Research
671 Foundation) – TRR 301 – project ID 428312742, in the subproject B02 "BISTUM" within the CRC

672 entitled "The Tropopause Region in a Changing Atmosphere" ("TPChange"). We also received
673 financial support by the "Dres. Göbel Climate-foundation".

674 **Figure captions**

675 **Figure** 1: Design of the UCASS and arrangement of its optical elements. Figure (a) shows the side
676 view of the UCASS, while figure (b) shows the front view. The definition of the particle detection
677 zone (df1) has been added to the figure. Adopted from Smith et al. (2019).

678 **Figure** 2: (a) The TFS housing ("c1"), which also contains the control and regulation electronics
679 of the TFS. The sensitive area of the TFS with a length of 6.9 mm is labelled as "c2". (b) The frontal
680 view of the experimental setup. The perspective is in the direction of flow towards the UCASS
681 front and into the flow tube, looking at the TFS and the Prandtl-Pitot tube, which is located
682 downstream behind the TFS.

683 **Figure** 3: Resulting flow velocity profiles along the elliptical cross-section of the instrument's
684 flow of the UCASS or of the TSF housing with a diameter of 40 mm × 30 mm (length × width).
685 Along the cross-section's main axis, the flow velocity measurements were carried out; twice for
686 an ambient flow velocity of ~ 5 m s^{-1} (forwards "a" and backwards "b", respectively) and once for
687 ~ 7 m s^{-1} (direction "b" only). Each data point represents an average of 15 velocity measurements.
688 The error bars, which are shown representatively in the bold-framed box, show the maximum
689 standard deviation for PPt's position (σ_{max} = 0.2 mm) and for all flow velocities measured with
690 the PPt (σ_{max} = 0.05 m s^{-1}). The position of the TFS (if installed) is marked by the grey area.

691 **Figure** 4: Measuring setup with UCASS, mounted TFS housing, and installed PPt (from the rear
692 reaching into the TFS housing), fixed in a vertically and horizontally tiltable apparatus with scales
693 for reading the deviation angles in each direction a) Side view in horizontal orientation b) Variable
694 deviation angles, which were set in angular degrees deviating from the zero position (iso-axial
695 case) during the experiments c) View of the measuring setup under horizontal and vertical
696 displacement from the zero position.

697 **Figure** 5: Comparison of the high-resolution calibration curve (HRC) with measurements of the
698 UCASS-implemented TFS 8 at variable angles of attack. The standard deviations of individual data
699 points are not shown for the sake of clarity.

700 **Figure** 6: Comparison of the recorded flow velocities outside (v_{TA}) and inside (v_{PPt}) the UCASS at
701 variable angles of attack during the series of measurements with TFS 8. The standard deviations
702 (at the most ± 0.1 m s^{-1} at tunnel wind speeds between 2 and 8 m s^{-1}) are not shown for reasons
703 of clarity. First-order polynomial fits were created for the flow velocities recorded under various
704 angles of attack to compare with the high-resolution calibration (HRC) at zero position (0°,0°).

705 **Figure** 7: Vertical profiles of the vertical velocity based on measurements of changed GPS and
706 barometric altitudes per unit time (i.e. v_{GPS} and v_p) and on TFS measurements of the flow velocity
707 (v_{TFS}^{corr}) through the UCASS of selected balloon soundings during a field mission together with
708 observed horizontal wind data (*u* and *v*) and the total wind speed (*u* + *v*) a-c) from 12 August,
709 launch at 14:10 (LT), d-f) from 16 August, launch at 11:51 (LT) and g-i) from 16 August, launch at
710 13:41 (LT). 10-seconds-running average of respective data are shown. Additionally, respective
711 deviations of the differently obtained flow velocities from each other are shown for each vertical
712 profile (panels b, e, h). Note that the deviation of the ascent rates (i.e. the external flow velocity,
713 GPS or *p*-based) in reference to the UCASS-internal flow speed differs from zero over large parts

714 of depicted flight sections. Occasional correlations of changing velocity ratios with changes in
715 wind speeds are recognizable, but a general causality cannot be identified.

716

717

718

719

720

721

722

723

724

725

726

727

728

729

730

731

732

733

734

735

736

737   Figures

738

757   Figure 1

758

759

Figure 2

783

784

785

786

787

788

789

790

791

792

793

794

795

796

797

798

799

Figure 3

800

801

802

803

804

805

Figure 4

Figure 5

853

854

855

856

857

858
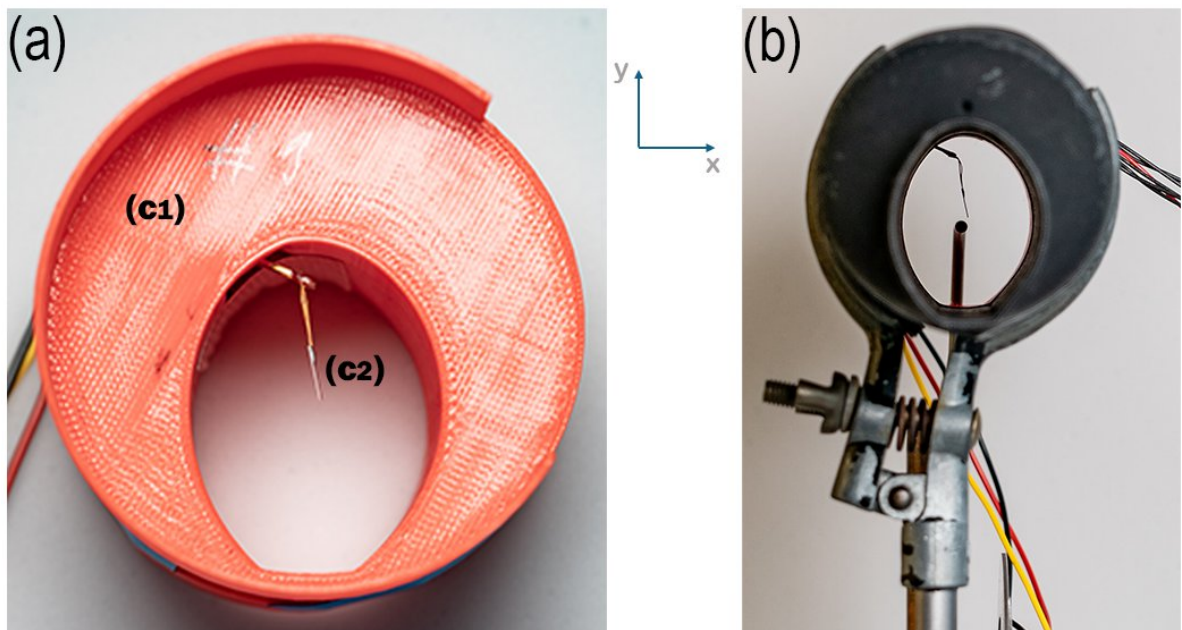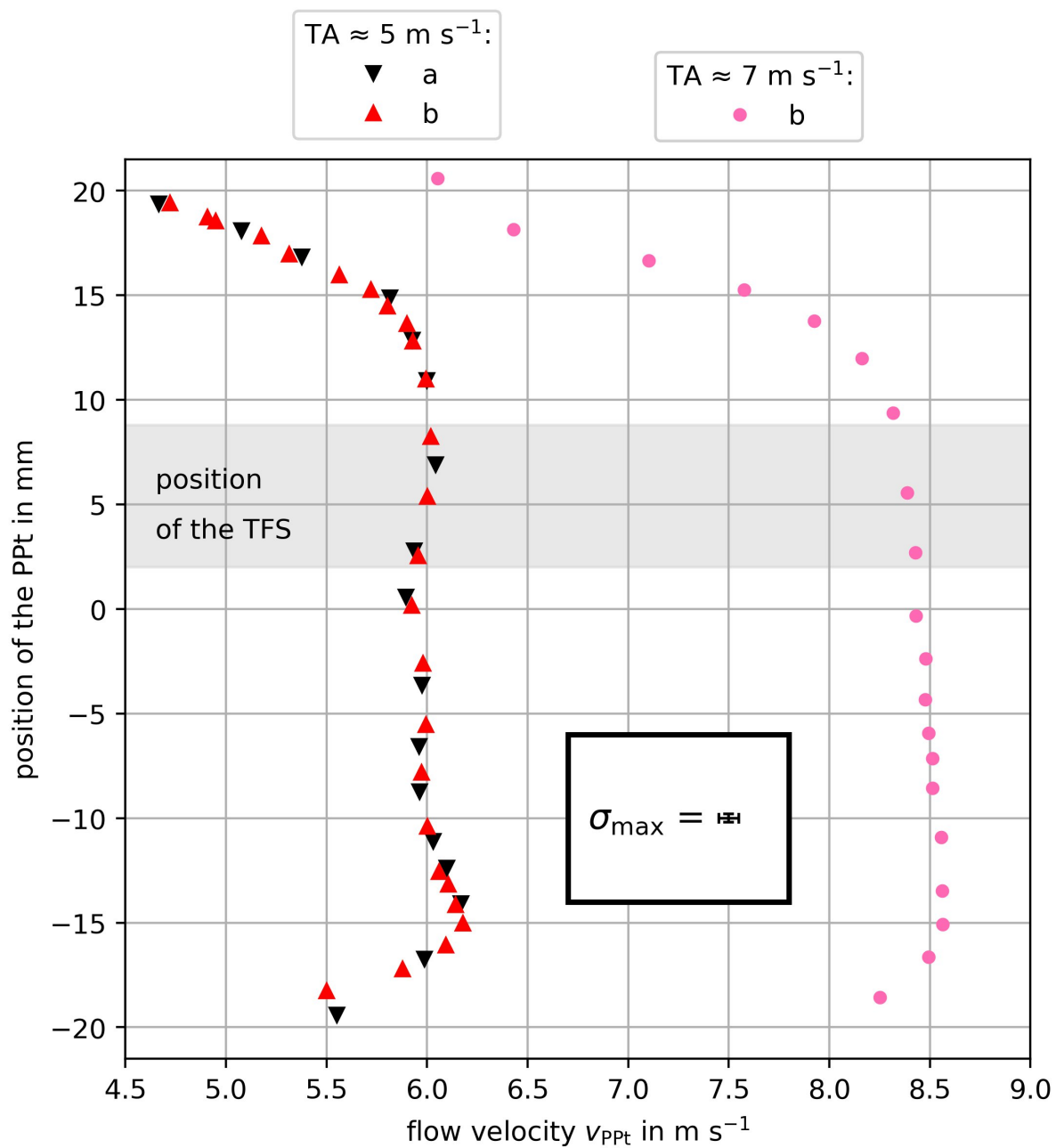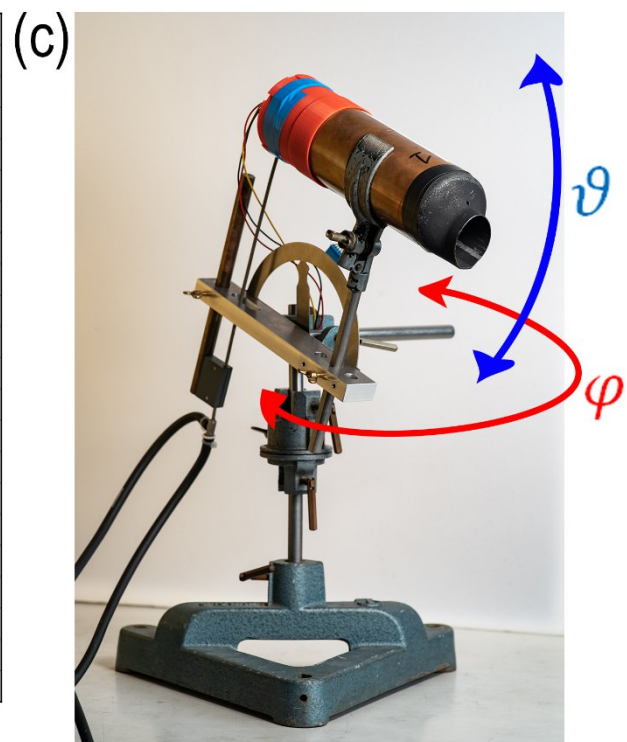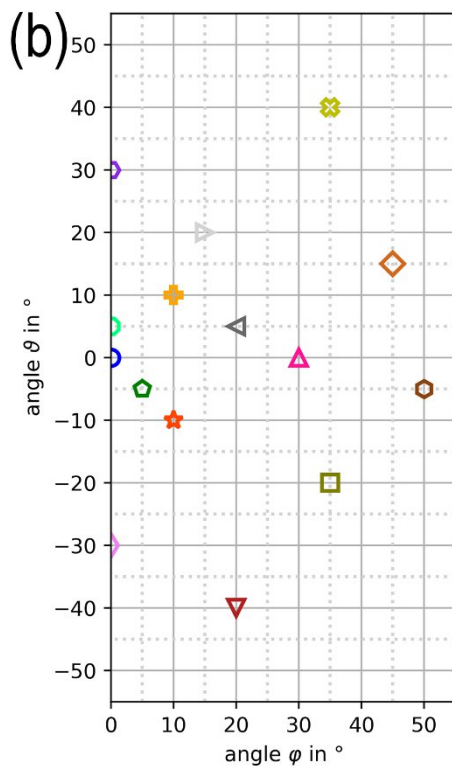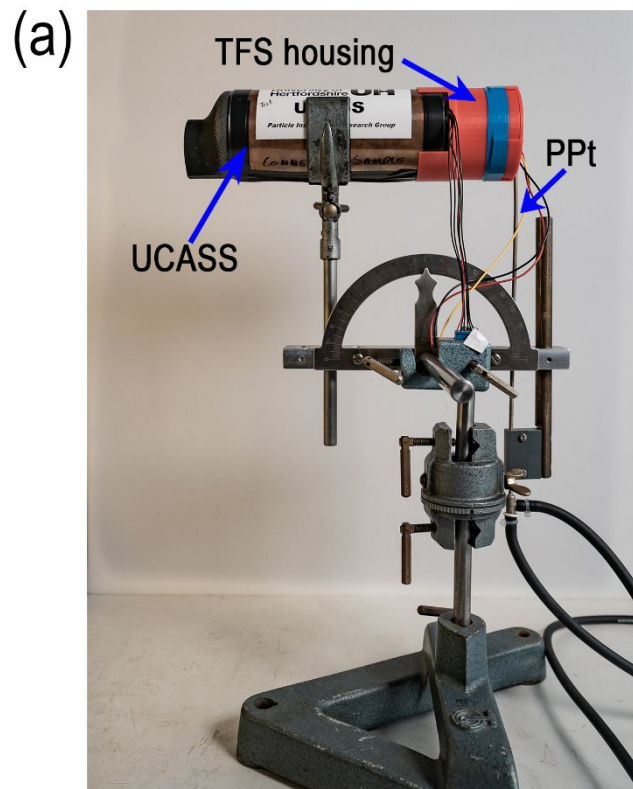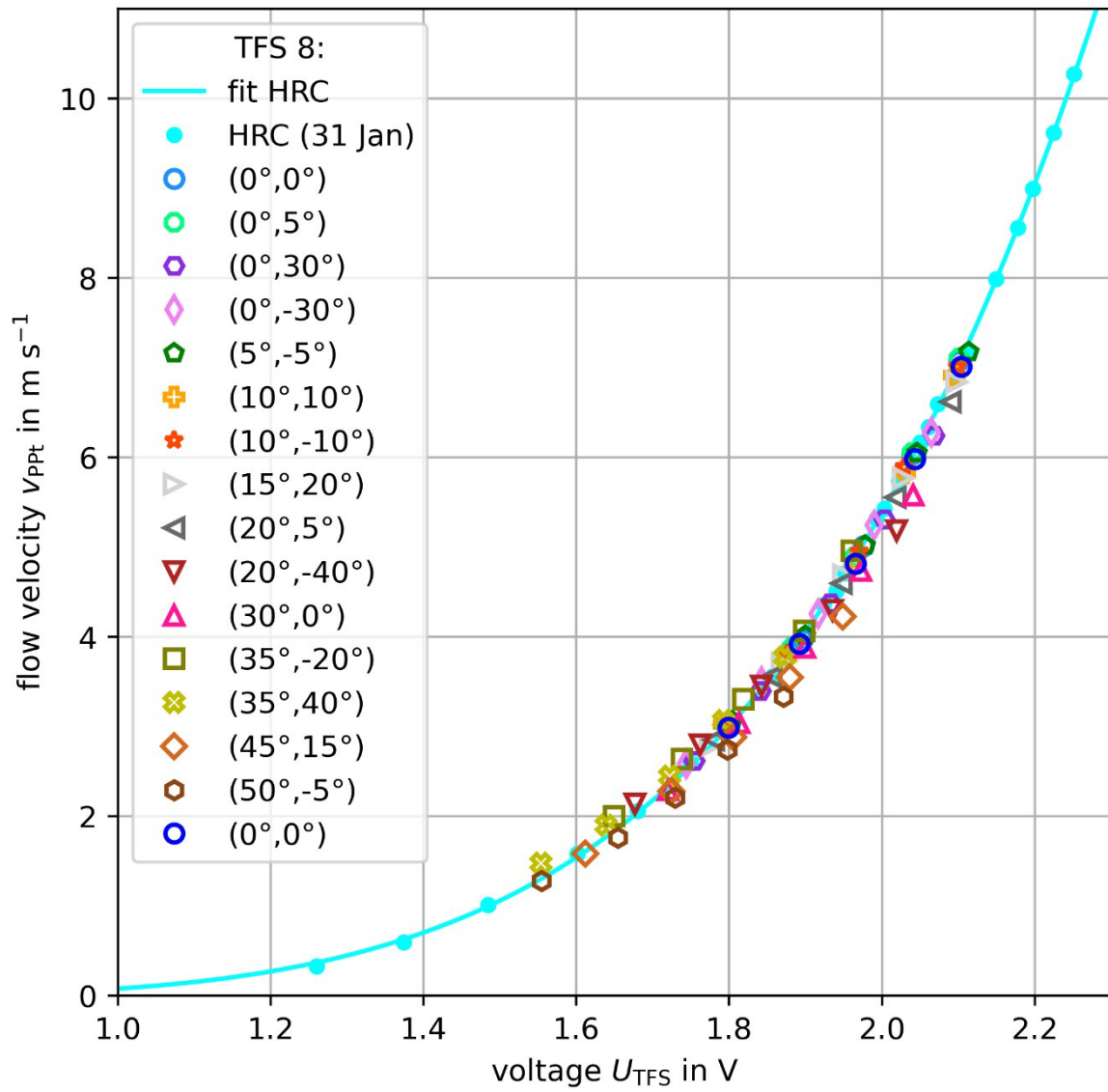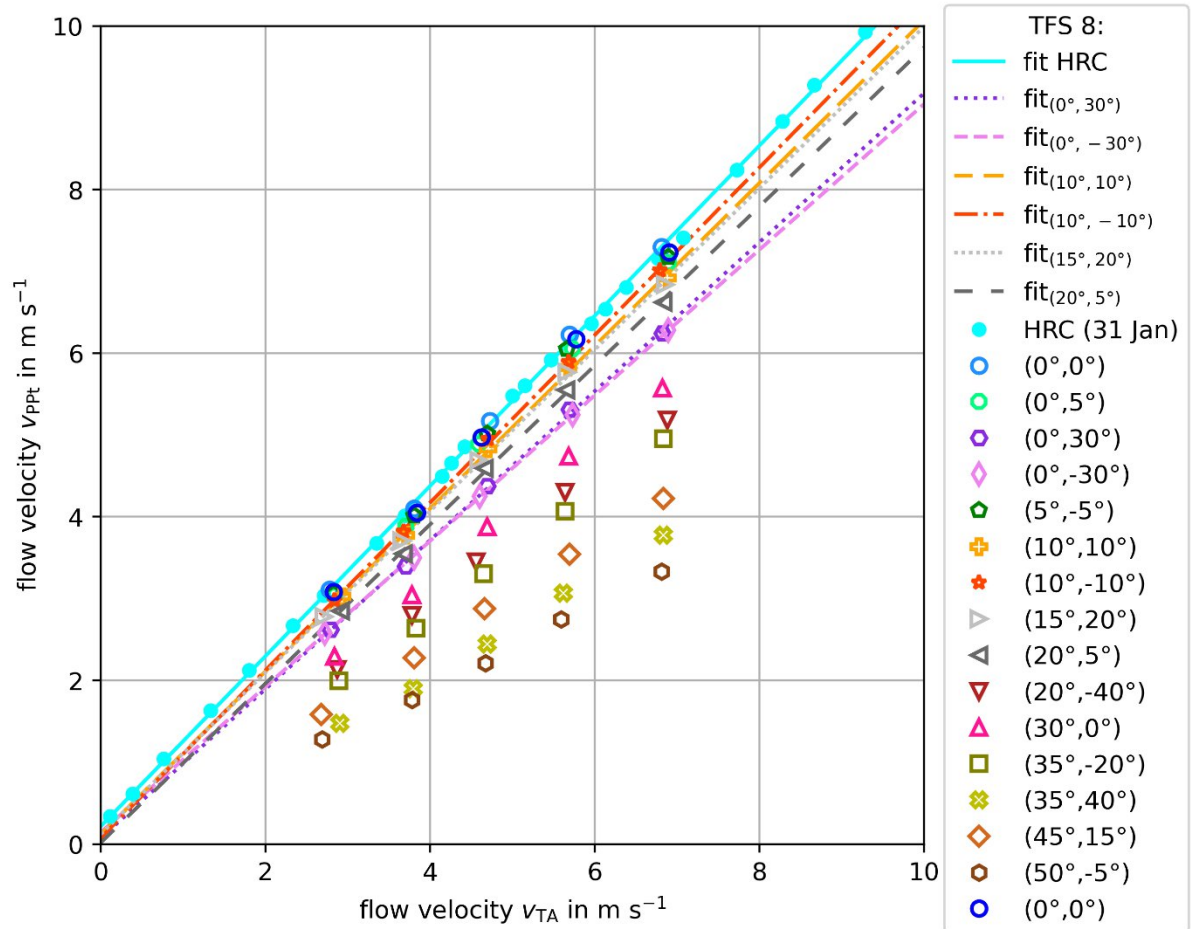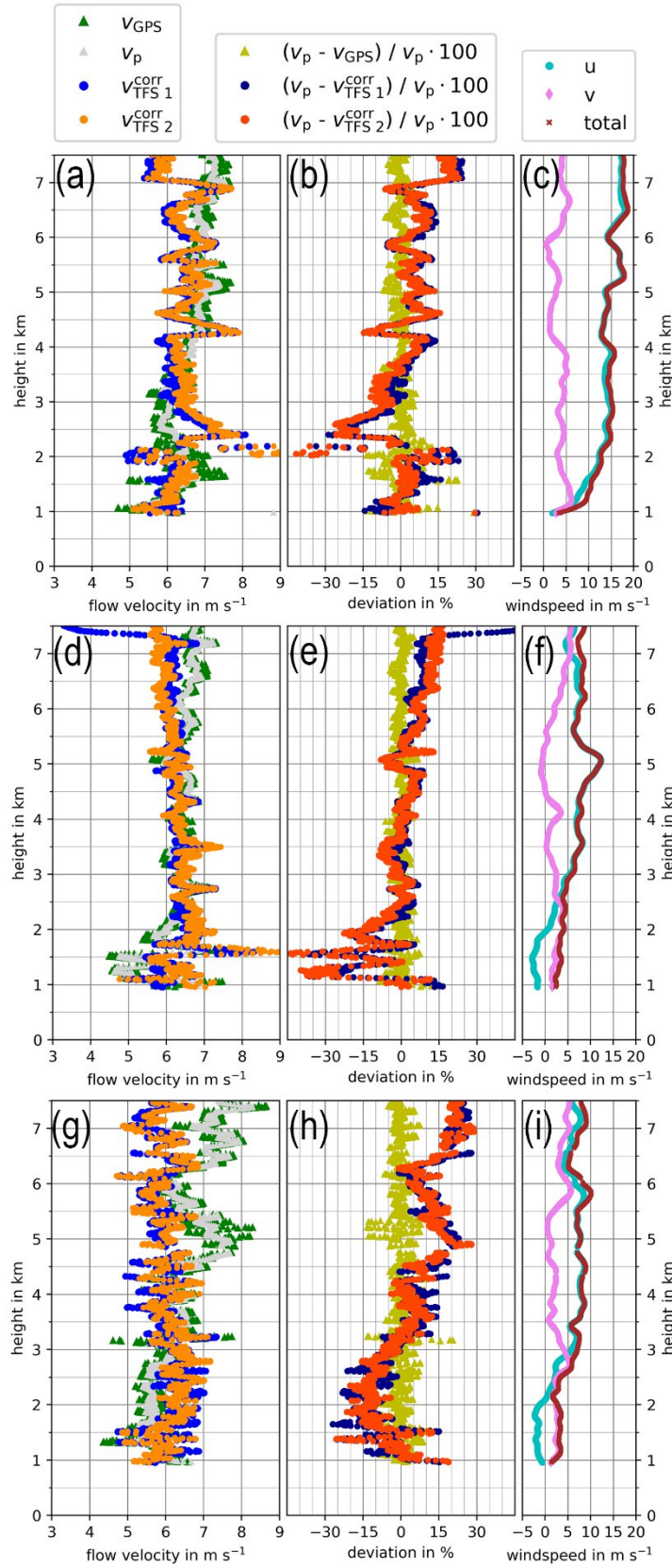
Figure 6

Figure 7

Tables

Exp. #	PPt	TFS/housing	description
1	yes	no/no	PPt in UCASS housing at position of detection region
2	yes	no/no	"—"
3	yes	yes/yes	PPt at detection region + attached TFS inside its housing
4	yes	yes/yes	"—"
5	yes	no/yes	PPt at TFS position inside TFS housing

Table 1

List of experiments (Exp.) conducted with the PPt at various positions inside the UCASS and TFS housing during wind tunnel flow calibrations.

fit	a	b
(0°,0°) HRC	1.040	0.216
(10°,10°)	0.995	0.119
(10°, -10°)	1.024	0.075
(15°,20°)	0.987	0.120
(20°,5°)	0.972	0.017
(0°, 30°)	0.910	0.073
(0°, -30°)	0.890	0.142

Table 2

Parameters of the linear fit function ($v_{PPt} = a \cdot v_{TA} + b$) to selected UCASS-internal flow velocities measured under variable angle of attack (AOA) in reference to the main wind tunnel flow speed.

angle (φ, ϑ)	deviation $\Delta v_{\text{rel}}^{\max}$ in %	deviation $\Delta \bar{v}_{\text{rel}}$ in %
(0°,0°)	1.1	0.6
(0°,5°)	1.7	1.0
(0°,30°)	3.5	1.8
(0°, -30°)	2.6	1.5
(5°, -5°)	1.5	1.0
(10°,10°)	2.8	0.9
(10°, -10°)	1.6	0.7
(15°,20°)	2.1	0.7
(20°,5°)	3.3	1.5
(20°, -40°)	8.6	4.9
(30°,0°)	7.3	4.1
(35°, -20°)	9.0	4.6
(35°,40°)	13.4	6.1
(45°,15°)	9.5	5.5
(50°, -5°)	10.6	6.7
(0°,0°)	1.4	1.0

Table 3

Maximum ($\Delta v_{\text{rel}}^{\max}$) and mean values ($\Delta \bar{v}_{\text{rel}}$) of the percentual relative deviation of measured flow velocities under variable angle of attack (AOA) for the calibration curve of TFS 8 (cf. Fig. 5).

angle (φ, ϑ)	deviation $\Delta v_{\text{rel}}^{\max}$ in %	deviation $\Delta \bar{v}_{\text{rel}}$ in %
(0°, 0°)	1.8	0.8
(0°, 5°)	4.6	3.3
(0°, 30°)	16.5	15.0
(0°, -30°)	16.1	15.3
(5°, -5°)	3.9	2.5
(10°, 10°)	7.3	6.2
(10°, -10°)	6.0	4.5
(15°, 20°)	8.4	7.0
(20°, 5°)	12.3	10.5
(20°, -40°)	33.4	31.1
(30°, 0°)	27.7	24.9
(35°, -20°)	38.1	35.1
(35°, 40°)	54.5	51.8
(45°, 15°)	47.2	44.1
(50°, -5°)	57.5	56.1
(0°, 0°)	3.8	2.1

Table 4

Maximum ($\Delta v_{\text{rel}}^{\max}$) and mean relative deviation ($\Delta \bar{v}_{\text{rel}}$) of in-UCASS measured flow velocity versus the wind tunnel flow speed as a function of the UCASS's angle of attack (AOA) in reference to velocity ratio in zero-position (in correspondence to measurements shown in Fig. 6).

T_{amb} and		275 ± 0.3 K	264 ± 0.3 K	254 ± 0.3 K
corresponding	h (Fig. 7a)	~3930-3990 m	~5700-5790 m	~7250-7310 m
heights	h (Fig. 7d)	~3690-3740 m	~5490-5560 m	~7250-7320 m
in soundings	h (Fig. 7g)	~3700-3770 m	~5400-5490 m	~7230-7300 m
RS41 SGP	Δp		± 1.0 hPa	
	ΔT	—	± 0.3 K	—
	Δh		± 10.0 gpm	
TFS	v_{TFS}^{corr} (Fig. 7a)	6.1 – 6.3 m s^{-1}	6.7 – 6.9 m s^{-1}	5.9 – 6.0 m s^{-1}
	v_{TFS}^{corr} (Fig. 7d)	6.3 – 6.4 m s^{-1}	6.1 – 6.3 m s^{-1}	5.8 m s^{-1}
	v_{TFS}^{corr} (Fig. 7g)	5.0 – 5.5 m s^{-1}	6.3 – 6.4 m s^{-1}	5.4 – 5.7 m s^{-1}
	Δv_{TFS}	± 0.4 %	± 0.4 %	± 0.4 %
	Δv_{TFS}^{corr}	**± 7.9 %**[*]	**± 8.8 %**[*]	**± 6.9 %**[*]
GPS	v_{GPS} (Fig. 7a)	6.7 m s^{-1}	6.7 m s^{-1}	7.6 m s^{-1}
	Δv_{GPS}	**-8.8 – -6.0 %**	| **0.0 – 3.5 %** |	**-29.3 – -27.7 %**
	v_{GPS} (Fig. 7d)	6.6 m s^{-1}	6.4 m s^{-1}	6.5 m s^{-1}
	Δv_{GPS}	| **-4.4 – -2.9 %** |	| **-4.5 – -1.4 %** |	**-14.2 – -12.5 %**
	v_{GPS} (Fig. 7g)	5.7 m s^{-1}	7.1 m s^{-1}	7.0 m s^{-1}
	Δv_{GPS}	**-14.1 – -4.2 %**	**-12.8 – -10.8 %**	**-30.8 – -23.2 %**

Table 5

Summarised uncertainties 1) ΔT, Δp, and Δh (GPS-altitude) from RS41 SGP radiosondes, 2) the overall uncertainty Δv_{TFS}^{corr} that result from Gaussian error propagation (Eq. 1 and Eq. 2) and that combine uncertainties from the RS41 SGP data and conditions during TFS calibrations (considering only ΔT, Δp, ΔT_0, and Δp_0) yielding Δv_{TFS} and b) the uncertainty (σ) in v_{TFS} obtained from cold chamber experiments (electronic supplement, Sect. S 1). 3) For three selected ambient temperature conditions (T_{amb} of 275 K, 264 K, and 254 K, from cold chamber experiments) the resulting deviations (Δv_{GPS}) of absolute v_{GPS} in reference to absolute v_{TFS}^{corr} from three vertical soundings (see Fig. 7 and adjacent text) are provided for comparison.

950   References

953   B+B-Thermo-Technik: Flow sensor element, FLW-122, data sheet, 0141 0316-88,
954   https://shop.bb-sensors.com/out/media/Datasheet_Flow_sensor_FLW-122_new.pdf (called 02
955   Sep. 2024), Donaueschingen, 2016, 2016.

957   Bearman, P. W.: Corrections for the effect of ambient temperature drift on hot-wire measurements
958   in incompressible flow DISA Info, Bull, 11, 25-30, 1971.

960   Bezantakos, S., Costi, M., Barmpounis, K., Antoniou, P., Vouterakos, P., Keleshis, C., Sciare, J., and
961   Biskos, G.: Qualification of the Alphasense optical particle counter for inline air quality monitoring,
962   Aerosol Sci Tech, 55, 361-370, https://doi.org/10.1080/02786826.2020.1864276, 2020.

964   Cardell, G.: A note on the temperature-dependent hot-wire calibration method of Cimbala and
965   Park, Exp Fluids, 14, 283-285, 1993.

967   Cimbala, J. M. and Park, W. J.: A direct hot-wire calibration technique to account for ambient-
968   temperature drift in incompressible-flow,, Exp Fluids, 8, 299-300,
969   https://doi.org/10.1007/BF00187234, 1990.

971   Dirksen, R. J., Bodeker, G. E., Thorne, P. W., Merlone, A., Reale, T., Wang, J., Hurst, D. F., Demoz, B.
972   B., Gardiner, T. D., Ingleby, B., Sommer, M., von Rohden, C., and Leblanc, T.: Managing the transition
973   from Vaisala RS92 to RS41 radiosondes within the Global Climate Observing System Reference
974   Upper-Air Network (GRUAN): a progress report, Geosci. Instrum. Method. Data Syst., 9, 337-355,
975   https://doi.org/10.5194/gi-9-337-2020, 2020.

977   EUFAR: European Facility for Airborne Research, https://www.eufar.net/aircrafts/list-matrix
978   (called 04 Dec. 2024), 2000.

980   Girdwood, J.: Optical measurement of airborne particles on unmanned aircraft, Ph.D. thesis,
981   University of Hertfordshire, Hatfield, UK, https://doi.org/10.18745/th.27277, 2023.

983   Girdwood, J., Stanley, W., Stopford, C., and Brus, D.: Simulation and field campaign evaluation of
984   an optical particle counter on a fixed-wing UAV, Atmos Meas Tech, 15, 2061-2076,
985   https://doi.org/10.5194/amt-15-2061-2022, 2022.

987   Golden, J. H., Serafin, R., Lally, V., and Facundo, J.: Atmospheric sounding systems, in: Mesoscale
988   meteorology and forecasting, edited by: Ray, P. S., American Meteorological Society, Boston, MA,
989   50-70, https://doi.org/10.1007/978-1-935704-20-1_4, 1986.

991   Guellouz, M. S. and Tavoularis, S.: A simple pendulum technique for the calibration of hot-wire
992   anemometers over low-velocity ranges, Exp Fluids, 18, 199-203,
993   https://doi.org/10.1007/BF00230265, 1995.
994

IPCC: International Panel on Climate Change; AR6 synthesis report: climate change 2023 (No. AR6), United Nations https://www.ipcc.ch/report/ar6/syr/, 2023.

Kandler, K., Benker, N., Bundke, U., Cuevas, E., Ebert, M., Knippertz, P., Rodriguez, S., Schütz, L., and Weinbruch, S.: Chemical composition and complex refractive index of Saharan mineral dust at Izana, Tenerife (Spain) derived by electron microscopy, Atmos Environ, 41, 8058-8074, https://doi.org/10.1016/j.atmosenv.2007.06.047, 2007.

Kasai, T., Tsuchiya, M., Takami, K., Hayashi, M., and Iwasaka, Y.: Balloon borne optical particle counter for stratospheric observation, Rev Sci Instrum, 74, 1082-1092, https://doi.org/10.1063/1.1533791, 2003.

Kezoudi, M., Tesche, M., Smith, H., Tsekeri, A., Baars, H., Dollner, M., Estellés, V., Bühl, J., Weinzierl, B., Ulanowski, Z., Müller, D., and Amiridis, V.: Measurement report: balloon-borne in situ profiling of Saharan dust over Cyprus with the UCASS optical particle counter, Atmos Chem Phys, 21, 6781-6797, https://doi.org/10.5194/acp-21-6781-2021, 2021.

Matsumura, T., Hayashi, M., Fujiwara, M., Matsunaga, K., Yasui, M., Saraspriya, S., Manik, T., and Suripto, A.: Observations of stratospheric aerosols by balloon-borne optical particle counter at Bandung, Indonesia, Journal of the Meteorological Society of Japan. Ser. II, 79, 709-718, https://doi.org/10.2151/jmsj.79.709, 2001.

Schön, M., Savvakis, V., Kezoudi, M., Platis, A., and Bange, J.: OPC-pod: a new sensor payload to measure aerosol particles for small uncrewed aircraft systems, Journal of Atmospheric and Oceanic Technology, 41, 499-513, https://doi.org/10.1175/JTECH-D-23-0078.1, 2024.

Smit, H. G. J., Poyraz, D., Van Malderen, R., Thompson, A. M., Tarasick, D. W., Stauffer, R. M., Johnson, B. J., and Kollonige, D. E.: New insights from the Jülich ozone sonde intercomparison experiment: calibration functions traceable to one ozone reference instrument, Atmos. Meas. Tech., 17, 73-112, https://doi.org/10.5194/amt-17-73-2024, 2024.

Smith, H. R., Ulanowski, Z., Kaye, P. H., Hirst, E., Stanley, W., Kaye, R., Wieser, A., Stopford, C., Kezoudi, M., Girdwood, J., Greenaway, R., and Mackenzie, R.: The Universal Cloud and Aerosol Sounding System (UCASS): a low-cost miniature optical particle counter for use in dropsonde or balloon-borne sounding systems, Atmos Meas Tech, 12, 6579-6599, https://doi.org/10.5194/amt-12-6579-2019, 2019.

Snels, M., Cairo, F., Di Liberto, L., Scoccione, A., Bracaglia, M., and Deshler, T.: Comparison of coincident optical particle counter and Lidar measurements of polar stratospheric clouds above McMurdo (77.85°S, 166.67°E) from 1994 to 1999, Journal of Geophysical Research: Atmospheres, 126, e2020JD033572, https://doi.org/10.1029/2020JD033572, 2021.

Sonntag, D.: Advancements in the field of hygrometry, Meteorol Z, 3(2), https://www.osti.gov/etdeweb/biblio/6907980, 1994.

Stier, P., van den Heever, S. C., Christensen, M. W., Gryspeerdt, E., Dagan, G., Saleeby, S. M., Bollasina, M., Donner, L., Emanuel, K., Ekman, A. M. L., Feingold, G., Field, P., Forster, P., Haywood, J., Kahn, R.,

1042   Koren, I., Kummerow, C., L'Ecuyer, T., Lohmann, U., Ming, Y., Myhre, G., Quaas, J., Rosenfeld, D.,
1043   Samset, B., Seifert, A., Stephens, G., and Tao, W.-K.: Multifaceted aerosol effects on precipitation,
1044   Nat Geosci, 17, 719-732, https://doi.org/10.1038/s41561-024-01482-6, 2024.
1045

1046   Vaisala: Radiosonde RS41-SGP, datasheet; https://docs.vaisala.com/v/u/B211444EN-J/en-US,
1047   2024.
1048

1049   Vömel, H. and Fujiwara, M.: Aerological measurements, in: Springer handbook of atmospheric
1050   measurements, edited by: Foken, T., Springer International Publishing, Cham, 1247-1280,
1051   https://doi.org/10.1007/978-3-030-52171-4_46, 2021.
1052

1053   Vömel, H. and Ingleby, B.: Chapter 2 - Balloon-borne radiosondes, in: Field measurements for
1054   passive environmental remote sensing, edited by: Nalli, N. R., Elsevier, 23-35,
1055   https://doi.org/10.1016/B978-0-12-823953-7.00010-1, 2023.
1056